# Cavity Controls Core-to-Core Resonant Inelastic X-Ray Scattering

S.-X. Wang,[1,2] Z.-Q. Zhao,[1] X.-Y. Wang,[1] T.-J. Li,[1] Y. Su,[1] Y. Uemura,[3] F. Alves Lima,[3] A. Khadiev,[4] B.-H. Wang,[4] J. M. Ablett,[5] J-P. Rueff,[5,6] H.-C. Wang,[7] O. J. L. Fox,[7] W.-B. Li,[8] L.-F. Zhu,[1] and X.-C. Huang[3,*]

[1]*Department of Modern Physics, University of Science and Technology of China, Hefei, Anhui 230026, China*
[2]*I. Physikalisches Institut, Justus-Liebig-Universität Gießen und Helmholtz Forschungsakademie Hessen für FAIR (HFHF) GSI Helmholtzzentrum für Schwerionenforschung Campus Gießen, Heinrich-Buff-Ring 16, 35392 Gießen, Germany*
[3]*European XFEL, 22869 Schenefeld, Germany*
[4]*Deutsches Elektronen-Synchrotron DESY, 22607 Hamburg, Germany*
[5]*Synchrotron SOLEIL, L'Orme des Merisiers, Départementale 128, 91190 Saint-Aubin, France*
[6]*Sorbonne Université, CNRS, Laboratoire de Chimie Physique—Matière et Rayonnement, LCPMR, F-75005 Paris, France*
[7]*Diamond Light Source, Harwell Science and Innovation Campus, Didcot, Oxfordshire OX11 0DE, United Kingdom*
[8]*MOE Key Laboratory of Advanced Micro-Structured Materials, Institute of Precision Optical Engineering (IPOE), School of Physics Science and Engineering, Tongji University, Shanghai 200092, China*

(Received 19 June 2025; revised 13 October 2025; accepted 9 January 2026; published 11 February 2026)

X-ray cavity quantum optics with inner-shell transitions has been limited by the spectral overlap between resonant and continuum states. Here, we report the first experimental demonstration of cavity-controlled core-to-core resonant inelastic x-ray scattering (RIXS). We suppress the absorption-edge effects by monitoring the RIXS profile, thereby resolving the resonant state from the overlapping continuum. We observe distinct cavity-induced energy shifts and cavity-enhanced decay rates in the $2p3d$ RIXS spectra of $WSi_2$. These effects, manifesting as stretched or shifted profiles in the RIXS planes, enable novel spectroscopic applications via cavity-controlled core-hole states. Our results establish core-to-core RIXS as a powerful tool to manipulate inner-shell dynamics in x-ray cavities, offering new avenues for integrating quantum optical effects with x-ray spectroscopy.

DOI: 10.1103/z6xz-p7cm

*Introduction*—X-ray quantum optics has become a rapidly evolving research field [1–4] driven by advancements in x-ray sources [5,6] and sample fabrication. In particular, thin-film planar cavities serve as a versatile platform for exploring quantum optical effects in the hard x-ray regime, enabling the observation of fundamental phenomena such as collective Lamb shift, superradiance, and strong light-matter coupling [7,8]. Cavities can modify the photonic density of states, thereby controlling the dynamics of excited states [9]. Initially, thin-film cavities were employed for Mössbauer nuclear transitions, exploiting their narrow linewidths and long coherence times [10–17]. More recently, they have been extended to manipulate inner-shell electronic transitions, which exhibit intriguing core-hole dynamics [18–23]. Notable advancements have been demonstrated, including spectral manipulation [18], observation of novel Fano profiles [22], control of core-hole lifetimes [19], and the formation of core polaritons [21]. Unlike the well-defined narrow transitions in Mösbauer nuclei [7,8] or other quantum systems [24,25], inner-shell excitations involve unique intermediate core-hole states characterized by multiple decay pathways, which in turn enable various modern x-ray spectroscopic techniques [4,26].

Core-hole states lie at the heart of core-level x-ray spectroscopies [27]. For example, core-hole dynamics play a crucial role in resonant inelastic x-ray scattering (RIXS), in which an incident x-ray excites a core electron to an unoccupied state and the system subsequently relaxes to the final state, emitting a photon of reduced energy and leaving behind an elementary excitation [28,29]. RIXS serves as a key probe of atomic, molecular, and condensed matter systems. These dynamics shape the temporal evolution of the scattering amplitude [30], control intensity ratios among elementary excitations [29,31], and modulate transition strengths between bound states [32], among other effects. The core-hole state has traditionally been regarded as an intrinsic property of matter, largely due to the lack of control over its decay channels. Recent advances, however, have demonstrated that both the decay rates and transition energies of inner-shell transitions can be tuned using x-ray cavities [18,19,23]. Integrating

*Contact author: xinchao.huang@xfel.eu

such cavity control with RIXS introduces new opportunities [4,26] for manipulating core-level interactions and expanding the scope of x-ray spectroscopy.

On the other hand, inner-shell resonances overlap with continuum states [4,18,19,22,23], which can obscure cavity-induced signatures in standard observables such as reflectivity and total fluorescence yield (TFY) measurements [12,15,33,34]. RIXS offers a promising approach to circumvent this limitation by exploiting resonant Raman processes to selectively probe resonant transitions [26]. Realizing x-ray cavity control over RIXS would therefore mark a significant step forward, enabling not only advanced spectroscopic applications but also new regimes of x-ray quantum optics. However, RIXS experiments face substantial challenges for signal detection due to their low scattering cross sections [35]. Achieving the high energy resolution needed to resolve subtle spectral features requires highly monochromatic x-rays and crystal analyzers with a relatively large radius of curvature. This combination makes RIXS a photon-hungry technique [28,29]. The integration of x-ray cavities (with ultrathin atomic layers) further tightens the photon budget by requiring highly collimated beams to enhance the cavity response at grazing angles [23,36–39]. Core-to-core RIXS denotes a process in which a deeper core hole created by x-ray absorption is refilled by another core electron; it is often termed resonant x-ray Raman scattering [29] or resonant x-ray emission (RXES) [40]. It offers comparatively higher scattering intensity owing to its two-step, dipole-allowed nature. This makes it the most promising approach for an initial demonstration of merging quantum optics with RIXS. Nonetheless, practical challenges remain, particularly in realizing grazing-incidence geometries required for efficient cavity coupling in the x-ray regime.

In this Letter, we report the first experimental demonstration of cavity control over core-to-core RIXS using a thin-film planar cavity. Guided by quantum Green's function theory [23,38,39], we designed the cavity to strongly modify the core-hole state. To probe this effect, we collected two-dimensional RIXS planes (maps of x-ray emission intensity versus incident and emitted photon energies), using a high-resolution energy-dispersive von Hamos (VH) spectrometer. Multiple crystal analyzers were used to increase the detection solid angle. We also benchmarked the setup by measuring the RIXS plane at a large incident angle in the absence of cavity effects. Subsequent measurements at two cavity detunings reveal hallmark quantum optical effects: a cavity-induced energy shift (CIS) and a cavity-enhanced decay rate (CER), both clearly observed in the RIXS plane as energy and intensity modulations. These observations open the door to advanced cavity-coupled x-ray spectroscopy based on core-to-core RIXS, including high energy resolution off-resonant spectroscopy (HEROS) [41] and high energy resolution fluorescence detected (HERFD) absorption spectroscopy [42]. Moreover, by isolating the resonant Raman feature at constant energy transfer [32,43], we circumvent the obscuring effects of absorption edge that typically accompany inner-shell transitions in hard x-ray quantum optics [18,19,22,23].

*Cavity effects on RIXS*—The nonseparable excitation and de-excitation steps in RIXS are described by the Kramers-Heisenberg formula [29]:

$$\frac{d^2\sigma}{d\Omega d\omega} = \sum_f \left| \sum_e \frac{\langle f|\overrightarrow{D'}|e\rangle\langle e|\vec{D}|g\rangle}{E_g+\omega_1-E_e-\delta_c+\frac{i\gamma}{2}} \right|^2 \times \delta(E_g+\omega_1-E_f-\omega_2). \quad (1)$$

Here $\omega_{1,2}$ are the energies of the incident and scattered photons, and $E_{g,e,f}$ denote the energies of the ground $|g\rangle$, intermediate (core-hole) $|e\rangle$, and final $|f\rangle$ states. The dipole operators $\vec{D}$ and $\vec{D'}$ govern the absorption and emission steps, respectively. Momentum-dependent effects are neglected because core-level states are typically nondispersive. The cavity-induced energy shift is captured by $\delta_c$, while $\gamma = \gamma_0 + \gamma_c$ includes the natural decay rate $\gamma_0$ and the cavity-enhanced contribution $\gamma_c$.

Figure 1(a) schematically illustrates the core-to-core RIXS process studied here: an incident x-ray of energy $\omega_1$ resonantly excites a $2p$ electron into an unoccupied state, and a $3d$ electron subsequently fills the core hole, emitting a photon of energy $\omega_2$, corresponding to the L$\alpha$ line of $WSi_2$, which is captured by the spectrometer as shown in Fig. 1(b). The energy transfer $\omega_1 - \omega_2$ reflects the excitation energy of the final state. Figure 1(c) presents a representative $2p3d$ RIXS plane of $WSi_2$ without cavity effects, plotted as a function of emitted photon energy (left panel, often termed RXES) and as a function of energy transfer (right panel, RIXS). In the latter representation, transitions to bound and continuum states are clearly distinguished. For resonant scattering, the energy transfer remains constant, giving rise to a vertical feature in the RIXS plane. Above the ionization threshold, however, the excited electron enters the continuum, and the subsequent decay emits x-rays with a nearly constant energy, yielding a diagonal feature.

The interaction of the x-ray cavity with inner-shell resonances is described by a quantum optical Green's-function model [23]. Figure 2 visualizes the control mechanism of the core-hole state for the cavity used in this work. The corresponding Green's-function expressions are given in the End Matter. The sample consists of 2.4-nm Pt/20.4-nm C/2.9-nm $WSi_2$/20.0-nm C/14.0-nm Pt, deposited on a silicon wafer, with $WSi_2$ serving as the resonant layer due to its strong $2p$–$5d$ dipole-allowed transition. Bulk-sample RIXS shows no additional splittings due to crystal-field or spin-orbit coupling [44]. Simulations show that the cavity-mode angle maximizes the CER, whereas the CIS reaches its maximum at an offset of $\Delta\theta \sim -70$ μrad. These two characteristic cavity

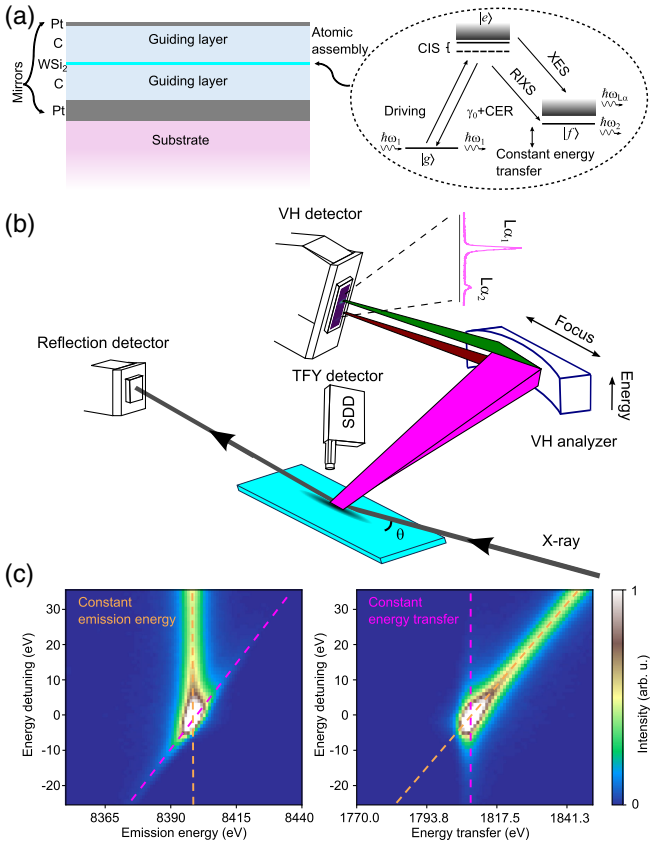


FIG. 1. Experimental scheme. (a) Cavity structure and RIXS energy-level diagram. Left: multilayer cavity composed of Pt mirrors, carbon (C) guiding layers, and a $WSi_2$ atomic ensemble. Right: simplified energy-level diagram for the core-to-core RIXS. The driving field resonantly excites the system to an intermediate core-hole state, which subsequently decays to the final state by emitting a characteristic x-ray. During the process, cavity effects induce an energy shift and an enhanced decay rate to the intermediate state. (b) Measurement geometry. The thin-film cavity sample is aligned at grazing incidence, resulting in a large footprint on the surface. A von Hamos (VH) spectrometer (energy resolution ~1 eV) disperses and focuses the emitted x-rays onto a 2D detector, recording energy-resolved spectral images. A silicon drift detector (energy resolution ~200 eV) collects the fluorescence in the vertical direction, while a downstream 2D detector monitors cavity reflectivity. (c) 2D RIXS planes shown as a function of emission energy (left) or energy transfer (right). A constant background, estimated from off-resonant spectral tails, has been subtracted. The incident angle (8.7 mrad) was set to be above the critical angle, a condition under which the x-ray can penetrate the sample; thus, the cavity effect is minimized. Pink dashed lines indicate the resonant Raman peaks at constant energy transfer, and yellow dashed lines mark the constant emission energy.

detunings were chosen for the experiment and are marked in Fig. 2.

*Scheme of RIXS measurement*—The x-ray thin-film planar cavity is operated at grazing-incidence angles (typically a few milliradians) to maintain high reflectivity

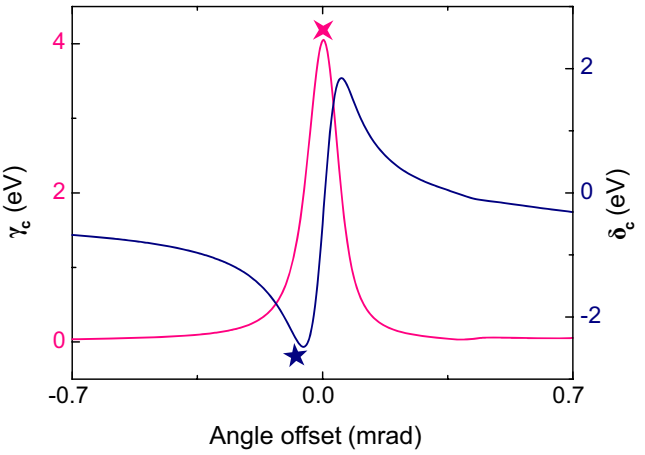


FIG. 2. The CER and CIS as a function of angle offset calculated by the quantum Green's function model. An angle divergence of 30 μrad is convoluted with the theoretical calculation. The pink cross and blue star indicate the specific angle offsets used in the experimental measurements, corresponding to the cavity-mode angle and an angle offset of −70 μrad, respectively.

of the mirror layers [45], resulting in an elongated beam footprint (>10 mm) and a line-like emission region on the sample. While such an extended footprint does not compromise conventional cavity observables recorded at a fixed angle (e.g., reflectivity or TFY) [10–19,22], RIXS measurements suffer from the defocusing and resolution loss in conventional analyzer geometries (e.g., Johann type [46] or DuMond type [47]). To minimize this limitation, we employed a von Hamos (VH) spectrometer [48,49] as illustrated in Fig. 1(b). The VH configuration uses a cylindrically bent crystal that disperses photon energies along the axial axis via Bragg diffraction while simultaneously focusing the signal along the bent direction. By aligning the elongated emission line with the focusing axis, the analyzer decouples the large beam footprint from the dispersion plane, thereby preserving the energy resolution (see [50] for details). The spectrometer resolves the $L\alpha_1$ and $L\alpha_2$ emission lines [inset of Fig. 1(b)], and we use the stronger $L\alpha_1$ line to record RIXS planes. Additional experimental details are given in the End Matter.

*Results and discussion*—Figure 3 presents the RIXS planes at the cavity mode (~3.5 mrad) and 70 μrad offset angle, respectively. Relative to the RIXS plane recorded at a large angle (8.7 mrad, Fig. 1(c)), we observe a remarkable energy shift and line-shape broadening. Note that in the large-angle reference, the resonant Raman peak (constant energy transfer, reflecting the core hole's natural width) is centered at zero detuning. The constant emission energy feature (yellow dashed line), oriented along the 45° diagonal, overlaps with the Raman signal (pink dashed line) near zero energy detuning, due to the emission linewidth and finite spectrometer resolution. Additionally, the absorption-edge step is slightly shifted—appearing as a

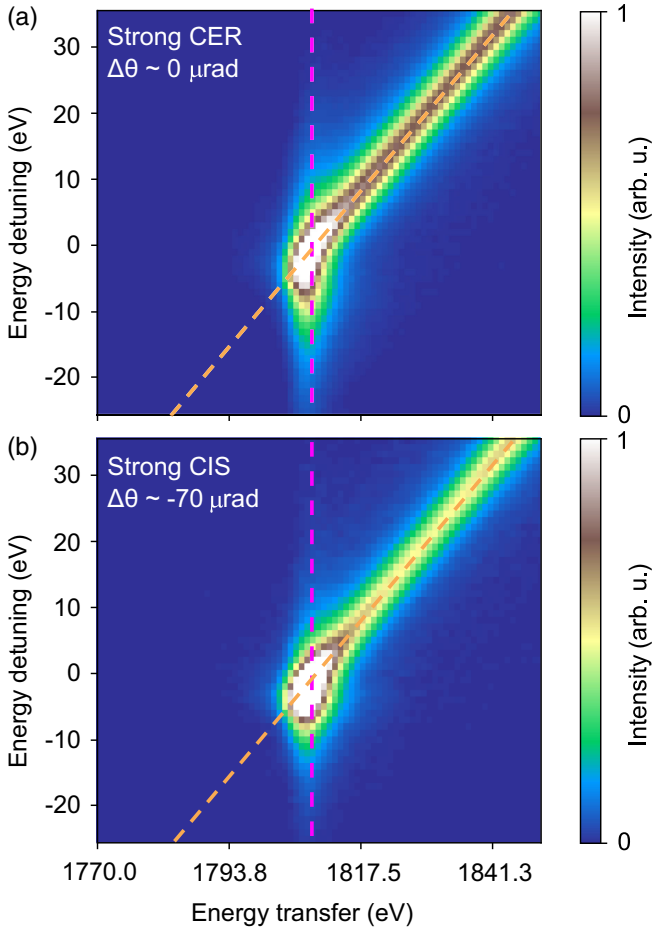


FIG. 3. The RIXS planes displayed as a function of energy transfer. (a) The incident angle is at the first order of the cavity mode, where CER is strong and CIS is weak. (b) The incident angle is set to have an offset of −70 μrad from (a), where CIS is strong and CER is weak. The vertical pink dashed lines indicate the peak intensities of the Raman feature.

small extension toward lower energy transfer. This observation is consistent with previous reports that showed the absorption edge shifted slightly above the white line transition, based on fits to TFY data [19,22,23].

At the cavity mode angle, the core-hole decay rate is strongly enhanced and the Raman profile is visibly stretched, as evidenced by extended tails on both sides of zero detuning energy in Fig. 3(a). The profile broadening is more pronounced towards lower energy due to a finite negative CIS. Additionally, the intensity of the constant emission energy feature increases significantly since the field inside the cavity is enhanced at the cavity mode, reflecting a standing wave effect [53]. Previous experiments that relied only on TFY [18,19,23], suffered from severe overlap between the resonant transition and the absorption edge. Here, however, the overlap is notably reduced since the Raman feature broadens primarily along the vertical (energy-transfer) axis due to cavity-enhanced decay ($\gamma_c$). Although the cavity effects on the transitions to continuum states remain under debate [19,23], any such effect is expected to be weaker than for the resonant transitions. These results clearly establish core-to-core RIXS as a sensitive probe for x-ray quantum optics involving inner-shell transitions. Furthermore, the broadened Raman tails carry additional spectroscopic information, enabling novel applications. For example, if the incident x-ray energy is fixed, a horizontal slice through the RIXS plane yields a spectrum that is sensitive to all final states reached from the same intermediate state (i.e., it isolates final states sharing that core-hole) [32,41]. The CER effect thus substantially improves the visibility of resonant transitions. Figure 3(b) shows a pronounced CIS, i.e., the Raman feature shifts to lower detuning energies and broadens slightly. Its overlap with the constant emission feature is further reduced since it moves further from the absorption edge. Such CIS can be exploited in HERFD x-ray absorption spectroscopy [42], where choosing a lower emission energy (negative $\delta_c$) enhances the

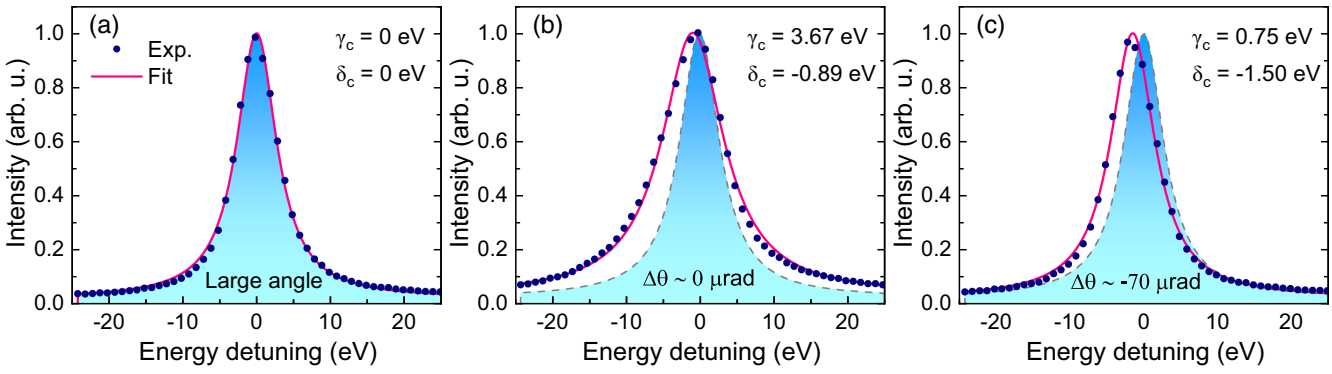


FIG. 4. The extracted resonant spectrum of the Raman feature. The spectra are integrated within a 2-eV band centered around the energy transfer peak in the corresponding RIXS plane. (a) The incident angle is at 0.5°. (b) The incident angle is close to the cavity mode angle ($\Delta\theta \sim 0$ μrad) and (c) detuned to an angle offset of about −70 μrad. Fits are performed using a Lorentzian function with a constant background. The shaded curves indicate the fitted profile of panel (a).

visibility of bound-state features without sacrificing intensity (see [50] for details).

To explicitly investigate the cavity effects, we isolated the Raman feature in the RIXS plane by integrating the intensities within a ±1-eV window (2-eV band in total) around the Raman maximum (pink dashed lines in Fig. 3). The resulting spectra are shown in Fig. 4 and were fitted with Lorentzian line profiles derived from Eq. (1). The large-angle measurement [Fig. 4(a)] provides the reference spectrum without cavity effects and is used to extract the cavity-induced shift $\delta_c$ and decay-rate enhancement $\gamma_c$ from the corresponding fits in Figs. 4(b) and 4(c). At the cavity mode angle, we observe a pronounced CER accompanied by a small CIS, consistent with theoretical predictions, whereas we find a larger CIS and reduced CER at an offset angle of $\Delta\theta = -70$ μrad. The measured CER and CIS are slightly smaller than predicted, likely because of a residual angular divergence introduced by curvatures in the sample surface, as well as uncertainty in the exact cavity alignment [50].

Additionally, the spectrum at the cavity mode angle in Fig. 4(b) shows a slight asymmetry relative to a Lorentzian profile. This deviation is not apparent at offset angles and is not captured by our current model. While various types of spectral asymmetries are known in quantum optics, such as Fano interference (e.g., [22] and references therein) and inhomogeneous atomic ensembles [54], the effect here may arise from the frequency-dependent response of the x-ray cavity itself [23], which has not, to our knowledge, been reported in the context of inner-shell transitions. Further measurements across both positive and negative cavity detunings will be required to clarify the underlying mechanism.

*Summary*—To summarize, we have presented the first measurement of core-to-core resonant inelastic x-ray scattering (RIXS) from an x-ray cavity sample. Transitions to the bound and continuum states, manifest as vertical and diagonal streaks in the RIXS planes, respectively. By comparing a large-angle reference (negligible cavity effects) with two cavity detunings selected to favor either a cavity-enhanced decay rate (CER) or a cavity-induced energy shift (CIS), we observe a pronounced spectral broadening of the Raman feature under a strong CER and a clear shift of the Raman peak to lower energies under a negative CIS.

Our findings highlight that core-to-core RIXS is a sensitive and selective probe for investigating x-ray cavity effects, particularly for distinguishing resonant bound-state transitions from continuum absorption edges. These results demonstrate that RIXS holds promise for exploring x-ray cavities with inner-shell transitions, drawing parallels to nuclear transitions in terms of collective effects [11,23] and Rabi splitting [15,55]. Moreover, our results underscore the potential of probing cavity effects via observables beyond elastic scattering (e.g., reflection and transmission) [23,36–39], suggesting that observables like conversion electron detection and secondary fluorescence [56] could offer comparable information and additional insights to nuclear transition systems [7,8]. Extended applications can also be envisioned. For example, it has been pointed out that cavity-controlled RIXS may help suppress intermediate-state dynamics, which could, in turn, facilitate more quantitative theoretical modeling of RIXS. Emerging x-ray sources, including diffraction-limited storage rings [6], seeded x-ray free-electron lasers [57], and attosecond x-ray pulses [58], now offer unprecedented photon coherence, brilliance, and degeneracy. These developments open new avenues, such as the interplay between x-ray cavity controlled effects and elementary excitations with lower energy transfer [29] and nonlinear x-ray phenomena [59].

*Acknowledgments*—The experiment was carried out with beam time approved by the GALAXIES beamline of SOLEIL synchrotron radiation facility (Proposal No. 20220927). The cavity sample was preliminarily tested with beam time at the B16 Test Beamline at the Diamond Light Source (Proposal No. MM31397). We acknowledge the support from Dr. Lingfei Hu (Diamond, now at USTC) during the B16 beamtime. We acknowledge the support of the National Natural Science Foundation of China through Grant No. 12334010, and the R&D HELIOS project at FXE of European XFEL. S.-X. W. acknowledges the support by the State of Hesse within the Research Cluster ELEMENTS (Project ID 500/10.006).

*Data availability*—The data that support the findings of this article are openly available [60].

[1] B. W. Adams, C. Buth, S. M. Cavaletto *et al.*, J. Mod. Opt. **60**, 2 (2013).
[2] E. Kuznetsova and O. Kocharovskaya, Nat. Photonics **11**, 685 (2017).
[3] L. J. Wong and I. Kaminer, Appl. Phys. Lett. **119**, 130502 (2021).
[4] S.-X. Wang, T.-J. Li, X.-C. Huang, and L.-F. Zhu, Acta Phys. Sin. **73**, 246101 (2024).
[5] C. Bostedt, S. Boutet, D. M. Fritz, Z. Huang, H. J. Lee, H. T. Lemke, A. Robert, W. F. Schlotter, J. J. Turner, and G. J. Williams, Rev. Mod. Phys. **88**, 015007 (2016).
[6] D. Einfeld, M. Plesko, and J. Schaper, J. Synchrotron Radiat. **21**, 856 (2014).
[7] R. Röhlsberger, J. Evers, and S. Shwartz, Quantum and nonlinear optics with hard X-rays, in *Synchrotron Light Sources and Free-Electron Lasers: Accelerator Physics, Instrumentation and Science Applications*, edited by E. J. Jaeschke, S. Khan, J. R. Schneider, and J. B. Hastings (Springer International Publishing, Cham, 2020), pp. 1399–1431, 10.1007/978-3-030-23201-6_32.
[8] R. Röhlsberger and J. Evers, Quantum optical phenomena in nuclear resonant scattering, in *Modern Mössbauer Spectroscopy: New Challenges Based on Cutting-Edge*

*Techniques*, edited by Y. Yoshida and G. Langouche (Springer, Singapore, 2021), pp. 105–171, 10.1007/978-981-15-9422-9_3.
[9] J. M. Raimond, M. Brune, and S. Haroche, Rev. Mod. Phys. **73**, 565 (2001).
[10] R. Röhlsberger, K. Schlage, T. Klein, and O. Leupold, Phys. Rev. Lett. **95**, 097601 (2005).
[11] R. Röhlsberger, K. Schlage, B. Sahoo, S. Couet, and R. Rüffer, Science **328**, 1248 (2010).
[12] R. Röhlsberger, H.-C. Wille, K. Schlage, and B. Sahoo, Nature (London) **482**, 199 (2012).
[13] K. P. Heeg, C. Ott, D. Schumacher, H.-C. Wille, R. Röhlsberger, T. Pfeifer, and J. Evers, Phys. Rev. Lett. **114**, 207401 (2015).
[14] K. P. Heeg, J. Haber, D. Schumacher, L. Bocklage, H.-C. Wille, K. S. Schulze, R. Loetzsch, I. Uschmann, G. G. Paulus, R. Rüffer, R. Röhlsberger, and J. Evers, Phys. Rev. Lett. **114**, 203601 (2015).
[15] J. Haber, X. Kong, C. Strohm, S. Willing, J. Gollwitzer, L. Bocklage, R. Rüffer, A. Pálffy, and R. Röhlsberger, Nat. Photonics **11**, 720 (2017).
[16] X.-C. Huang, W.-B. Li, X.-J. Kong, and L.-F. Zhu, Opt. Express **25**, 31337 (2017).
[17] S. Velten, L. Bocklage, X. Zhang, K. Schlage, A. Panchwanee, S. Sadashivaiah, I. Sergeev, O. Leupold, A. I. Chumakov, O. Kocharovskaya *et al.*, Sci. Adv. **10**, eadn9825 (2024).
[18] J. Haber, J. Gollwitzer, S. Francoual, M. Tolkiehn, J. Strempfer, and R. Röhlsberger, Phys. Rev. Lett. **122**, 123608 (2019).
[19] X.-C. Huang, X.-J. Kong, T.-J. Li, Z.-R. Ma, H.-C. Wang, G.-C. Liu, Z.-S. Wang, W.-B. Li, and L.-F. Zhu, Phys. Rev. Res. **3**, 033063 (2021).
[20] M. Vassholz and T. Salditt, Sci. Adv. **7**, eabd5677 (2021).
[21] B. Gu, A. Nenov, F. Segatta, M. Garavelli, and S. Mukamel, Phys. Rev. Lett. **126**, 053201 (2021).
[22] Z.-R. Ma, X.-C. Huang, T.-J. Li, H.-C. Wang, G.-C. Liu, Z.-S. Wang, B. Li, W.-B. Li, and L.-F. Zhu, Phys. Rev. Lett. **129**, 213602 (2022).
[23] X.-C. Huang, T.-J. Li, F. A. Lima, and L.-F. Zhu, Phys. Rev. A **109**, 033703 (2024).
[24] R. Blatt and C. F. Roos, Nat. Phys. **8**, 277 (2012).
[25] A. Blais, A. L. Grimsmo, S. M. Girvin, and A. Wallraff, Rev. Mod. Phys. **93**, 025005 (2021).
[26] F. Gel'mukhanov, M. Odelius, S. P. Polyutov, A. Föhlisch, and V. Kimberg, Rev. Mod. Phys. **93**, 035001 (2021).
[27] F. De Groot and A. Kotani, *Core Level Spectroscopy of Solids* (CRC Press, Taylor & Francis, London, 2008), 10.1201/9781420008425.
[28] A. Kotani and S. Shin, Rev. Mod. Phys. **73**, 203 (2001).
[29] Luuk J. P. Ament, M. van Veenendaal, T. P. Devereaux, J. P. Hill, and J. van den Brink, Rev. Mod. Phys. **83**, 705 (2011).
[30] F. Gel'mukhanov and H. Ågren, Phys. Rep. **312**, 87 (1999).
[31] G. Ghiringhelli, M. Matsubara, C. Dallera, F. Fracassi, R. Gusmeroli, A. Piazzalunga, A. Tagliaferri, N. B. Brookes, A. Kotani, and L. Braicovich, J. Phys. Condens. Matter **17**, 5397 (2005).
[32] M. L. Baker, M. W. Mara, J. J. Yan, K. O. Hodgson, B. Hedman, and E. I. Solomon, Coord. Chem. Rev. **345**, 182 (2017).
[33] K. P. Heeg, H.-C. Wille, K. Schlage, T. Guryeva, D. Schumacher, I. Uschmann, K. S. Schulze, B. Marx, T. Kämpfer, G. G. Paulus, R. Röhlsberger, and J. Evers, Phys. Rev. Lett. **111**, 073601 (2013).
[34] X. Kong and A. Pálffy, Phys. Rev. Lett. **116**, 197402 (2016).
[35] W. Schülke, *Electron Dynamics by Inelastic X-Ray Scattering* (Oxford University Press, New York, 2007), 10.1093/oso/9780198510178.001.0001.
[36] K. P. Heeg and J. Evers, Phys. Rev. A **88**, 043828 (2013).
[37] K. P. Heeg and J. Evers, Phys. Rev. A **91**, 063803 (2015).
[38] X. Kong, D. E. Chang, and A. Pálffy, Phys. Rev. A **102**, 033710 (2020).
[39] D. Lentrodt, K. P. Heeg, C. H. Keitel, and J. Evers, Phys. Rev. Res. **2**, 023396 (2020).
[40] F. De Groot, Chem. Rev. **101**, 1779 (2001).
[41] W. Błachucki, J. Szlachetko, J. Hoszowska, J.-C. Dousse, Y. Kayser, M. Nachtegaal, and J. Sá, Phys. Rev. Lett. **112**, 173003 (2014).
[42] M. Bauer, Phys. Chem. Chem. Phys. **16**, 13827 (2014).
[43] F. M. F. de Groot, P. Glatzel, U. Bergmann, P. A. van Aken, R. A. Barrea, S. Klemme, M. Hävecker, A. Knop-Gericke, W. M. Heijboer, and B. M. Weckhuysen, J. Phys. Chem. B **109**, 20751 (2005).
[44] Z. Q. Zhao, S. X. Wang, X. Y. Wang, Y. Su, Z. R. Ma, X. C. Huang, and L. F. Zhu, Acta Phys. Sin. **74**, 183201 (2025).
[45] R. Röhlsberger, T. Klein, K. Schlage, O. Leupold, and R. Rüffer, Phys. Rev. B **69**, 235412 (2004).
[46] H. H. Johann, Z. Phys. **69**, 185 (1931).
[47] J. W. M. DuMond, Rev. Sci. Instrum. **18**, 626 (1947).
[48] L. v. Hámos, Ann. Phys. (Berlin) **409**, 716 (1933).
[49] A. Wach, J. Sá, and J. Szlachetko, J. Synchrotron Radiat. **27**, 689 (2020).
[50] See Supplemental Material at http://link.aps.org/supplemental/10.1103/z6xz-p7cm for experimental details and potential applications. Supplemental Material includes Refs. [51,52].
[51] M. Björck and G. Andersson, J. Appl. Crystallogr. **40**, 1174 (2007).
[52] K. Hämäläinen, D. P. Siddons, J. B. Hastings, and L. E. Berman, Phys. Rev. Lett. **67**, 2850 (1991).
[53] J. Zegenhagen and A. Kazimirov, *The X-Ray Standing Wave Technique* (World Scientific, Singapore, 2013), 10.1142/6666.
[54] P. Andrejić and A. Pálffy, Phys. Rev. A **104**, 033702 (2021).
[55] J. Haber, K. S. Schulze, K. Schlage, R. Loetzsch, L. Bocklage, T. Gurieva, H. Bernhardt, H.-C. Wille, R. Rüffer, I. Uschmann, G. G. Paulus, and R. Röhlsberger, Nat. Photonics **10**, 445 (2016).
[56] R. Röhlsberger, *Nuclear Condensed Matter Physics with Synchrotron Radiation: Basic Principles, Methodology and Applications* (Springer Science & Business Media, New York, 2004), 10.1007/b86125.
[57] S. Liu, C. Grech, M. Guetg, S. Karabekyan, V. Kocharyan, N. Kujala, C. Lechner, T. Long, N. Mirian, W. Qin *et al.*, Nat. Photonics **17**, 984 (2023).
[58] J. Yan, W. Qin, Y. Chen, W. Decking, P. Dijkstal, M. Guetg, I. Inoue, N. Kujala, S. Liu, T. Long *et al.*, Nat. Photonics **18**, 1293 (2024).
[59] N. Rohringer, Phil. Trans. R. Soc. A **377**, 20170471 (2019).

[60] S.-X. Wang, Z.-Q. Zhao, X.-Y. Wang, T.-J. Li, Y. Su, Y. Uemura, F. Alves Lima, A. Khadiev, B.-H. Wang, J. M. Ablett, J.-P. Rueff, H.-C. Wang, O. J. L. Fox, W.-B. Li, L.-F. Zhu, and X.-C. Huang, 10.5281/zenodo.17992570 (2025).

[61] J. M. Ablett, D. Prieur, D. Céolin, B. Lassalle-Kaiser, B. Lebert, M. Sauvage, T. Moreno, S. Bac, V. Balédent, A. Ovono, M. Morand, F. Gélebart, A. Shukla, and J.-P. Rueff, J. Synchrotron Radiat. **26**, 263 (2019).

## End Matter

*Cavity control mechanisms*—The cavity-induced energy shift (CIS) $\delta_c$ and cavity-enhanced decay rate (CER) $\gamma_c$ of the intermediate core-hole state follow from the real and imaginary parts of the cavity Green's function [23]. In the collective description, the corresponding spin-exchange $J$ and decay rate $\Gamma$ are

$$J = \frac{N}{A}\mu_0\omega^2\mathbf{d}^* \cdot \mathrm{Re}[\mathbf{G}(z, z', \omega)] \cdot \mathbf{d}, \tag{A1}$$

$$\Gamma = \frac{2N}{A}\mu_0\omega^2\mathbf{d}^* \cdot \mathrm{Im}[\mathbf{G}(z, z', \omega)] \cdot \mathbf{d}. \tag{A2}$$

Here, $N/A$ is the atomic areal density, $\mathbf{d}$ is the dipole matrix element, and $\mathbf{G}(z, z', \omega)$ is the normalized electromagnetic Green's function of the multilayer cavity, evaluated using a transfer matrix or Parratt formalism [23]. The strong dependence of $\mathbf{G}$ on the angular detuning $\Delta\theta$ from the first-order cavity mode enables control of $\delta_c$ and $\gamma_c$, as summarized in Fig. 2.

*Experimental setups*—Before the RIXS measurements, the performance and structure of the cavity sample were characterized at the B16 Test Beamline of Diamond Light Source (see [50]), which provides similar incident-beam conditions. The RIXS measurements were performed at the GALAXIES beamline of the SOLEIL synchrotron [61]. A vertically collimated x-ray beam (divergence ~30 μrad, size ~60 μm) illuminated the sample, which was positioned using a hexapod system for precise angular scans. Reflected x-rays were collected by a forward 2D detector, while fluorescence passing through a pinhole was recorded by a silicon drift detector in the vertical direction. The cavity mode angles were identified from reflectivity [50], and the corresponding TFY spectra were used for validation of the emission data [50]. Eight von Hamos analyzers were employed to increase the detection solid angle [50], and the emitted x-rays were imaged on a dedicated 2D detector.